


## Article

# MnO<sub>2</sub>@Corncob Carbon Composite Electrode and All-Solid-State Supercapacitor with Improved Electrochemical Performance

Xin-Sheng Li, Man-Man Xu, Yang Yang, Quan-Bo Huang, Xiao-Ying Wang , Jun-Li Ren and Xiao-Hui Wang \* 

State Key Laboratory of Pulp and Paper Engineering, South China University of Technology, Guangzhou 510640, China

\* Correspondence: fewangxh@scut.edu.cn; Tel.: +86-20-87111735

Received: 6 June 2019; Accepted: 15 July 2019; Published: 26 July 2019



**Abstract:** Two corncob-derived carbon electrode materials mainly composed of micropores (activated carbon, AC) and mesopores/macropores (corncob carbon, CC) were prepared and studied after the anodic electrodeposition of MnO<sub>2</sub>. The capacity of the MnO<sub>2</sub>/activated carbon composite (MnO<sub>2</sub>@AC) electrode did not noticeably increase after MnO<sub>2</sub> electrodeposition, while that of the MnO<sub>2</sub>/corncob carbon composite (MnO<sub>2</sub>@CC) electrode increased up to 9 times reaching 4475 mF cm<sup>-2</sup>. An asymmetric all-solid-state supercapacitor (ASC) was fabricated using AC as the anode, MnO<sub>2</sub>@CC as the cathode, and polyvinyl alcohol (PVA)/LiCl gel as the electrolyte. An ultrahigh specific capacitance of 3455.6 mF cm<sup>-2</sup> at 1 mA cm<sup>-2</sup>, a maximum energy density of 1.56 mW h cm<sup>-2</sup>, and a long lifetime of 10,000 cycles can be achieved. This work provides insights in understanding the function of MnO<sub>2</sub> in biomass-derived electrode materials, and a green path to prepare an ASC from waste biomass with excellent electrochemical performance.

**Keywords:** natural biomass; porous carbon; architecture; MnO<sub>2</sub>; supercapacitor

## 1. Introduction

Carbonaceous materials derived from abundant waste biomass (sugarcane bagasse, potato, lotus seedpod, rice husk, taro epidermis, banana peel, mulberry leaves, coffee grounds, etc.) [1–8] are considered as good electrode materials for supercapacitors due to their high specific surface area, good conductivity, easy accessibility, low cost, and renewability. However, biomass-based supercapacitors suffer from slow charge/discharge performances and a limited energy density because of their micropore structure, which limit their application in high-performance supercapacitors [9].

It has been recognized that a rational microstructure design and the inclusion of active materials are two effective approaches to improve the capacitance performance of biomass-derived carbon materials [10–12]. Microstructure design mainly pays attention to constructing a hierarchical pore structure of the carbon material using improved pretreatment and carbonization processes [13], while the other strategies concentrate on the introduction of pseudocapacitive materials such as heteroatoms [14,15], conducting polymers [16,17], transition metal sulfides [18], and oxides [19–24]. Among these pseudocapacitive materials, manganese dioxide (MnO<sub>2</sub>) is the most promising one due to its high theoretical specific capacitance (1370 F g<sup>-1</sup>), wide potential window, rich reserves, and being environmentally friendly [25].

Anchoring MnO<sub>2</sub> on carbon substrates such as activated carbon (AC) using electrochemical deposition offers an effective way to obtain a superior capacitive property and rate capability [26–31]. Zhang et al. prepared an electrodeposited MnO<sub>2</sub>@AC composite air cathode with a power density of

1554 mW m<sup>-2</sup>, which was 1.5 times that of an AC air cathode [32]. In some other reports, the mass-specific capacitance of MnO<sub>2</sub>@AC electrode was raised by 105.8% [33] or even three times [34] that of AC electrode. However, the application of the MnO<sub>2</sub> functionalized biomass-derived carbon materials in all-solid-state supercapacitors (ASC), which are essential for the next-generation portable electronics, still remains a challenge due to limited performance of the device.

In this work, high performance electrode materials were prepared from corncob carbon using the carbonization and electrodeposition of MnO<sub>2</sub>. It was interesting to find that the performance of corncob carbon (CC) without chemical activation was significantly improved after MnO<sub>2</sub> deposition. The obtained MnO<sub>2</sub>@CC electrode showed a high area-specific capacitance of 4475 mF cm<sup>-2</sup>, which was 9 times that of CC. Highly porous and conductive corncob AC was also obtained, although its performance could not be greatly improved via MnO<sub>2</sub> deposition. A sandwich-structured ASC utilizing corncob AC as an anode, MnO<sub>2</sub>@CC as a cathode, polyvinyl alcohol (PVA)/LiCl gel as an electrolyte, and a thin sulfonated membrane as separator was fabricated. The device demonstrates high power/energy density and shows great potential in green and renewable energy storage for its reliability and good biocompatibility.

## 2. Materials and Methods

### 2.1. Materials

The corncob raw materials were collected in Henan province in the middle of China. Polytetrafluoroethylene (PTFE) solution was purchased from Aladdin Chemistry Co., Ltd. (Shanghai, China). A membrane filter (MPF50AC) separator was purchased from Nippon Kodoshi Plant of Japan (Kochi-ken, Japan). Acetylene black and nickel foam were obtained from Lili Lithium Electric Technology Center (Taiyuan, China). Hydrochloric acid (HCl) and potassium hydroxide (KOH) were analytical grade chemical reagents used without purifying. Manganese acetate (Mn(CH<sub>3</sub>COO)<sub>2</sub>) and lithium chloride (LiCl) were provided by the Fuchen Chemical Reagent Factory (Tianjin, China). Sodium sulfate (Na<sub>2</sub>SO<sub>4</sub>) was purchased from Runjie Chemical Reagent Company (Shanghai, China). We purchased polyvinyl alcohol (PVA-124) from Sinopharm Chemical Reagent Co., Ltd (Shanghai, China); it had a molecular weight of 105,000, degree of polymerization in the range from 2400 to 2500, and a hydrolysis degree of 98–99%.

### 2.2. Synthesis of AC and CC

AC was prepared using one-step carbonization. The dried corncob was chopped into 5–10 cm pieces using a disintegrator. After that, solid KOH was mixed with corncob residues at a KOH/carbon mass ratio of 0.5 and a small amount of water was added to just cover the corncob residues. After being soaked in KOH solution for 10 h, the corncob residues were dried at 80 °C for 12 h and further carbonized at 750 °C for 1.5 h with a heating rate of 3 °C min<sup>-1</sup> in an argon atmosphere. The carbonized samples were washed several times using 1 M HCl and deionized (DI) water, then vacuum-dried overnight. Finally, the corncob-based porous carbons could be created.

CC was prepared without the activation of KOH. The dried natural corncob was cut into the desired size (2 cm × 1 cm) along the axial direction and then pre-carbonized at 300 °C for 1 h with a heating rate of 5 °C min<sup>-1</sup> in an argon atmosphere, followed by carbonization at 900 °C for 1 h with a heating rate of 6.7 °C min<sup>-1</sup>. Then, the obtained solid biochar was washed successively using DI water and the moisture was removed to obtain the final CC.

### 2.3. Preparation of AC and CC Electrodes

The AC electrode was prepared as follows. The AC pieces were ground into AC power in an agate mortar. Then, 1 g AC power was added to 30 mL water and the mixture solution was stirred magnetically for 0.5 h at ambient temperature. A homogeneous dispersion was obtained by sonicating the mixture for several hours. A total of 0.125 g carbon black and 0.125 g PTFE (mass ratio

of AC/carbon/PTFE = 8:1:1) were added into the beaker under magnetic stirring and sonicating in order. After that, the mixture was dried into a viscous slurry at 100 °C in the vacuum oven. Finally, the mixed slurry was pressed into a membrane and pasted on the nickel foam (1 cm × 2 cm), followed by vacuum drying to get the final AC electrodes.

The cleaned CC were used as the electrode directly due to its self-supporting and excellent electrical conductivity.

#### 2.4. Preparation of MnO<sub>2</sub>@AC and MnO<sub>2</sub>@CC Electrodes

MnO<sub>2</sub> was grown in situ on an AC electrode with a typical anodizing method performed in the electrochemical station (CH Instruments Ins, Shanghai, China). Electrodeposition was achieved by using a platinum (Pt) plate and Ag/AgCl electrode as a counter electrode and reference electrode [34], respectively. Before electrodeposition, the obtained AC electrode (1 cm × 1 cm) was soaked in the electrolyte containing 0.1 M of Mn(CH<sub>3</sub>COO)<sub>2</sub> and 0.1 M of Na<sub>2</sub>SO<sub>4</sub> for one night. A constant current of 1 mA/cm<sup>2</sup> was applied to ensure the growth of MnO<sub>2</sub> nanosheets on the AC membrane and its channels when the deposition time changed from 5 min to 2 h. Next, the as-prepared samples were rinsed gently by the water and vacuum dried at 60 °C to obtain the final MnO<sub>2</sub>@AC electrodes.

The preparation of MnO<sub>2</sub>@CC electrodes was similar to that of MnO<sub>2</sub>@AC electrodes except for the difference that the CC block was clamped by a couple of platinum sheets, which made sure there was a uniform distribution of current to support the growth of the MnO<sub>2</sub> nanosheets.

#### 2.5. Fabrication of All-Solid-State ASCs

The PVA/LiCl gel electrolyte was prepared as follows: 6.3 g of LiCl and 30 mL of DI water were added in the beaker and stirred for 5 min to get the transparent solution. Next, 3 g PVA was added into the solution, followed by an oil bath with magnetic stirring at 90 °C for 1 h to dissolve the PVA.

In a typical assembling process of ASCs, the AC anode, MnO<sub>2</sub>@CC cathode, and membrane filter were soaked in the PVA/LiCl electrolyte for 5 min and then coagulated in a vacuum oven at room temperature overnight. After that, the ASCs were constructed by pressing the AC anode and MnO<sub>2</sub>@CC cathode together with a membrane filter (MPF50AC) between them.

#### 2.6. Material Characterization

The microstructure of these samples were investigated using scanning electron microscopy (SEM, ZEISS Merlin, Oberkochen, Germany) and transmission electron microscopy (TEM, JEM-2100, JEOL Ltd., Tokyo, Japan). The crystalline structure of the electrode materials was determined using an X-ray diffractometer (XRD, D/max-III A with nickel-filtered Cu K $\alpha$  radiation ( $\lambda$  = 0.15418 nm), Rigaku Corporation, Tokyo, Japan). X-ray photoelectron spectroscopy (XPS) was conducted on an AMICUS (Shimadzu, Japan) spectrometer with monochromated Mg K $\alpha$  radiation. The nitrogen sorption measurements were carried out using an ASAP 2020 analyzer (Micromeritics, Georgia, GA, USA). The Raman spectra were recorded on a Raman Spectrometer (HORIBA Jobin Yvon, Paris, France).

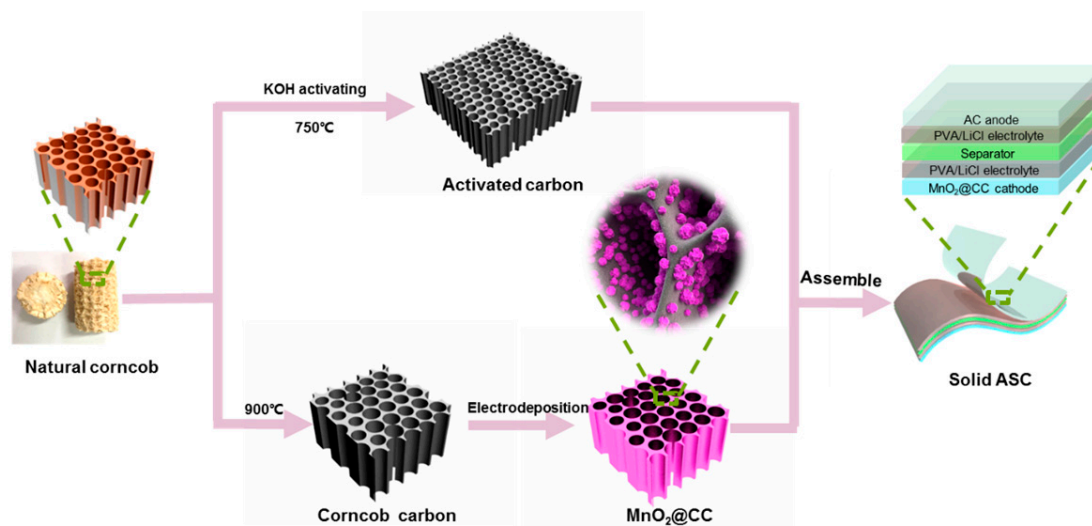
#### 2.7. Electrochemical Characterization

The electrochemical behavior of a single electrode was studied using a three-electrode mode in 1 M Na<sub>2</sub>SO<sub>4</sub> aqueous solution. Cyclic voltammetry (CV) measurements were carried out to evaluate the capacitive behavior of the AC and CC. Galvanostatic charge/discharge (GCD) curves were tested to calculate the specific capacitance of AC and CC. An external window voltage of −1 V to 0 V and 0–0.8 V, which correspond to AC- and CC-based electrodes, respectively, were applied in the charging and discharging process. Cycling stability was tested using a land-battery testing system.

### 3. Results

#### 3.1. Morphological Analysis

Herein, two different porous carbon materials: AC and CC were prepared from the agricultural byproduct corncob, as shown in Scheme 1. AC was prepared using KOH activation and carbonization of chopped corncob pieces, while CC was obtained via direct carbonization of chopped corncob pieces without activation. The morphology of natural corncob tissue, AC, and CC are presented in Figure S1. The natural corncob has a rich vascular tissue with tracheids and vessels for transporting water and nutrients, which endows it with natural open channels. Figure S1a shows the SEM images of the natural corncob, where 3D vertical channels (10–30  $\mu\text{m}$ ) can be observed. With KOH activation, the original geometry of the natural corncob was destructed. A loose and highly porous structure with a large amount of micropores was created (Figure S1b). Unlike AC, the original vertical channel structure of the natural corncob could be well-kept in CC, whose channel diameter was between 30 to 60  $\mu\text{m}$  (Figure S1c). Besides the major tunnels, there were also many small channels (1–3  $\mu\text{m}$ ) on the inner wall of the macroporous channels (Figure S1d), which constituted a hierarchical pore structure. In most cases, the micropores endow the material with a high specific surface area and large specific capacitance, while the mesopores and macropores can facilitate the transportation of electrolytes [35].



**Scheme 1.** Different routes to prepare corncob-based carbon electrodes and the construction process of an ASC.

To improve the capacitive performance of AC and CC, a constant current of  $1 \text{ mA cm}^{-2}$  was applied to them to grow  $\text{MnO}_2$  in situ. Figure 1 shows the morphology and structure of AC and CC with electrodeposited  $\text{MnO}_2$  for different durations. Due to the high conductivity of AC and CC ( $0.02 \Omega/\text{sq}$ ),  $\text{MnO}_2$  was easily electrodeposited in the substrate. Figure 1a shows that the pores in AC had been filled with  $\text{MnO}_2$  crystals with only 5 min of deposition, which induced a blocking of channels and the destruction of pore structures. The deposited  $\text{MnO}_2$  crystals presented a nanoflower shape (Figure 1b), which is similar to previous reports [36–38]. With a prolonged deposition time, the  $\text{MnO}_2$  crystals grew into a more uniform and smooth film (Figure S2). After 120 min, a very flat and continuous  $\text{MnO}_2$  crystals film had been obtained, while the crystal shape was almost unchanged (Figure S2c).

On the other hand, as Figure 1c shows, the pore structure of CC was well-preserved in  $\text{MnO}_2@\text{CC}$ . Figure S3 shows the morphology of  $\text{MnO}_2@\text{CC}$  with increased deposition time from 30 min to 10 h. As the deposition time increased, the thickness of the channel wall increased gradually, resulting in a reduction of the channel diameter. After manganese dioxide was electrodeposited on CC for 2 h, the pore wall became thicker (10  $\mu\text{m}$ ), but the vertical channels were still unimpeded. With a layer of



manganese dioxide nanosheets (Figure 1d) growing on the inner and outer surfaces of the pore wall, the original small pore on the inner pore wall disappeared. When the electrodeposition lasted up to 5 h, the  $\text{MnO}_2$  crystals penetrated throughout the tunnels, while the surface of  $\text{MnO}_2@\text{CC}$  still remained unimpeded according to the cross-sectional view image (Figure S4c). When the deposition time reached up to 10 h (Figure S3g), stacked  $\text{MnO}_2$  crystals separated by criss-crossed cracks appeared on the surface, probably due to the inhomogeneous nuclei growth. In summary, a very short electrodeposition time (5 min) led to the clogging of pores in  $\text{MnO}_2@\text{AC}$ , while  $\text{MnO}_2@\text{CC}$  could keep the original macroporous structure over a long electrodeposition time of up to 2 h. The difference in the growth rate of  $\text{MnO}_2$  crystals in the two materials was probably determined by their different surface areas. Smaller pore structures and larger specific surface area (SSA) lead to a higher current density and the faster growth of  $\text{MnO}_2$  crystals.

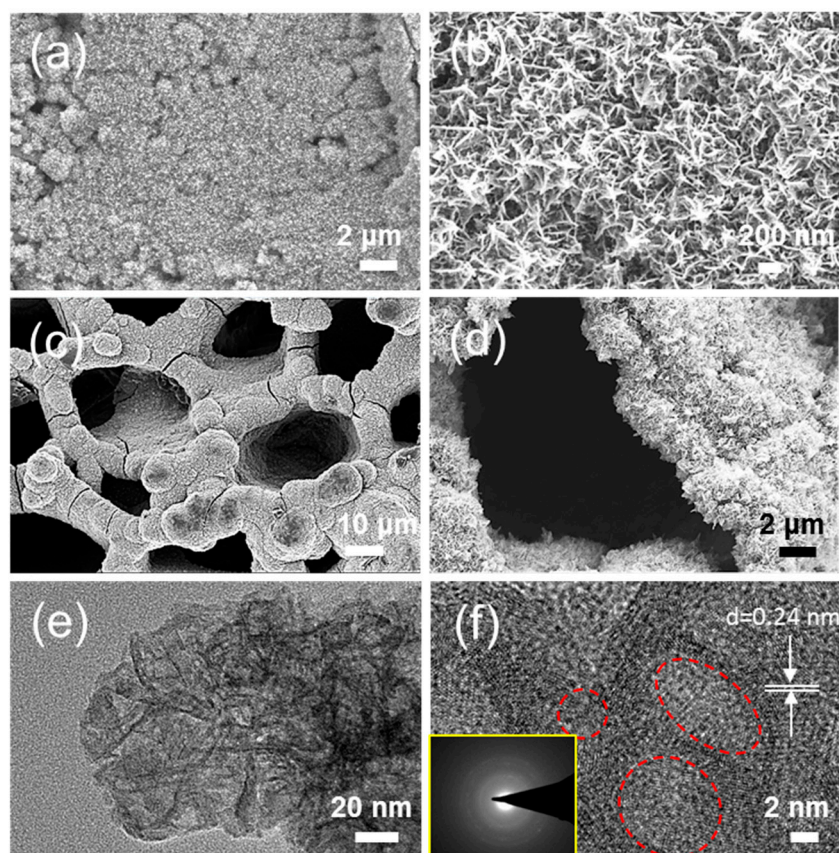


**Figure 1.** (a,b) SEM and HR-SEM images of  $\text{MnO}_2@\text{AC}$ -5 min, respectively. (c,d) SEM and HR-SEM images of  $\text{MnO}_2@\text{CC}$ -2 h, respectively. (e,f) TEM and HR-TEM images (inset: selected-area electron diffraction (SAED) pattern) of  $\text{MnO}_2@\text{CC}$ -2h, respectively.

The detailed microstructure of the electrodeposited  $\text{MnO}_2$  in  $\text{MnO}_2@\text{CC}$ -2 h was characterized using high resolution TEM. Figure 1e shows that the individual  $\text{MnO}_2$  nanoflower was composed of interconnected sheet-like subunits with a thickness of several nanometers. Meanwhile, it can be seen that there were some small disordered or defective regions and spaces ranging from 5 nm to 14 nm on the  $\text{MnO}_2$  nanosheets (red circles in Figure 1f). The corresponding selected-area electron diffraction (SAED) pattern (inset of Figure 1f) demonstrated that the deposited  $\text{MnO}_2$  was polycrystalline. Furthermore, the lattice spacings of 0.7 nm and 0.24 nm correspond to the interplanar distances of (001) and  $(\bar{1}11)$  planes of  $\delta\text{-MnO}_2$ , respectively. XRD results confirmed this (Figure S5a). As shown, the two broad peaks around  $23^\circ$  and  $43.6^\circ$  correspond to the (002) and (100) diffraction planes of porous carbon, respectively. Apart from them, new peaks appeared at  $36.7^\circ$  and  $65.7^\circ$ , which correspond to the

diffraction of  $(\bar{1}11)$  and  $(311)$  planes of  $\delta$ - $\text{MnO}_2$ . The weak intensity and the broad width of two peaks indicate the poor crystallinity of layered  $\delta$ - $\text{MnO}_2$ .

To further demonstrate the change in microstructure of the corncob-based materials after depositing  $\text{MnO}_2$ , the nitrogen adsorption–desorption isotherms and pore size distribution using the Barrett–Joyner–Halenda (BJH) method were investigated. According to Figure 2a–d, the isotherms of these porous materials all present typical type IV isotherms and the pore size distribution curves confirm the hierarchical porosity. The sharp increase (Figure 2b) at a low relative pressure ( $P/P^0 = 0.06$ – $0.4$ ) is characteristic of micropores. AC contained far more micropores than  $\text{MnO}_2$ @AC. The specific surface area ( $S_{\text{BET}}$ ) of AC decreased from  $626.08 \text{ m}^2 \text{ g}^{-1}$  to  $32.76 \text{ m}^2 \text{ g}^{-1}$  after the  $\text{MnO}_2$  electrodeposition. These results prove that the micropores were blocked after  $\text{MnO}_2$  was electrodeposited. The appearances of hysteresis demonstrated the existence of mesopores. Meanwhile, a sharp upward tendency (Figure 2d) at high partial pressures ( $P/P^0 = 0.4$ – $1.0$ ) signified that there were many macropores in CC and  $\text{MnO}_2$ @CC. The  $S_{\text{BET}}$  of  $\text{MnO}_2$ @CC was  $3.5 \text{ m}^2 \text{ g}^{-1}$ , which was close to that of CC ( $5.2 \text{ m}^2 \text{ g}^{-1}$ ). This result indicates that the macropores structure in CC was not obviously affected by  $\text{MnO}_2$  loading. Figure 2e,f graphically illustrates the architecture of AC and CC after electrodepositing  $\text{MnO}_2$ . For AC,  $\text{MnO}_2$  crystals were grown not only on the surface but also inside the micropores, even with a very short electrodeposition time of 5 min, resulting in a very clogged microstructure. For CC, due to its macroscopic pore structure, the deposition of  $\text{MnO}_2$  was much slower and did not significantly change its microstructure.

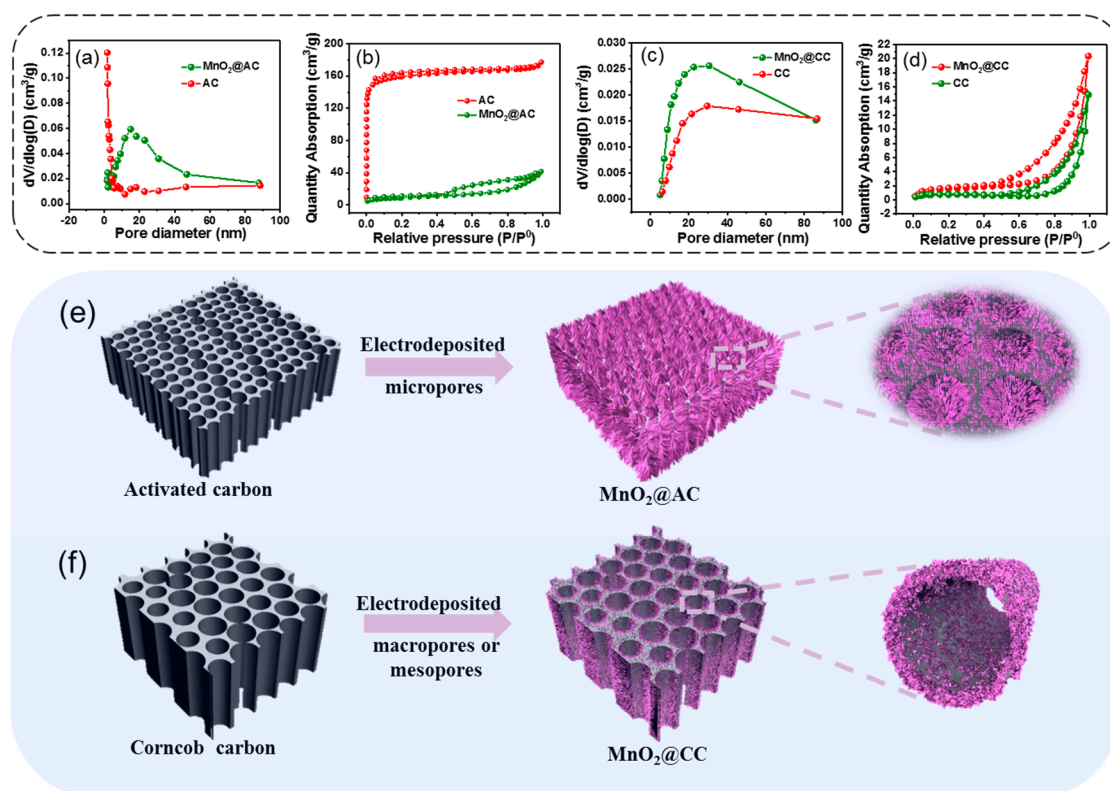


**Figure 2.** (a,c) The pore size distribution curves of AC and CC, respectively. (b,d) Nitrogen adsorption–desorption isotherms of  $\text{MnO}_2$ @AC and  $\text{MnO}_2$ @CC, respectively. (e,f) Schematic illustration depicting the architecture of AC and CC with electrodeposited  $\text{MnO}_2$ , respectively.

### 3.2. Element Analysis and Surface Chemistry Characterization

Figure S5b represents the Raman spectrum of the corncob-derived materials. The two peaks located at  $1350 \text{ cm}^{-1}$  and  $1580 \text{ cm}^{-1}$  belong to the D and G bands, respectively. The G band was the in-plane vibration of graphitic carbon while the D band was ascribed to structural defects [39]. The  $I_D/I_G$  intensity

ratio provides the degree of disorder and the average size of the  $sp^2$  domains. The  $I_D/I_G$  ratio of AC,  $MnO_2@AC$ , CC,  $MnO_2@CC$  were 0.87, 0.93, 1.00, and 0.97 respectively, which means they all had typical amorphous carbon structures. The  $I_D/I_G$  ratio of CC was higher than AC, which may be due to the higher carbonization temperature.

The XPS spectra of  $MnO_2@AC$  and  $MnO_2@CC$  composites in Figure 3 show that C, Mn, and O were the dominant elements in the samples. In the C 1s spectrum, three peaks located at 284.7 eV, 285.1 eV, and 288.5 eV corresponded to the C–C/C=O bond, C–O bond, and C=O band, respectively. In addition, the XPS spectrum of O 1s (Figure 3c,e) was resolved into three components, indicating the coexistence of a Mn–O–Mn bond (529.9 eV), Mn–O–H bond (531.2 eV), and H–O–H bond (532.2 eV). Two obvious peaks appeared in the Mn 2p spectra (Figure 3f) at 653.9 eV and 642.1 eV that corresponded to Mn 2p<sub>3/2</sub> and Mn 2p<sub>1/2</sub>, respectively. The spin-energy separation of the two peaks was 11.8 eV, further proving that the Mn oxidation state in the  $MnO_2@AC$  and  $MnO_2@CC$  composite was  $Mn^{4+}$  ( $MnO_2$ ) [40].

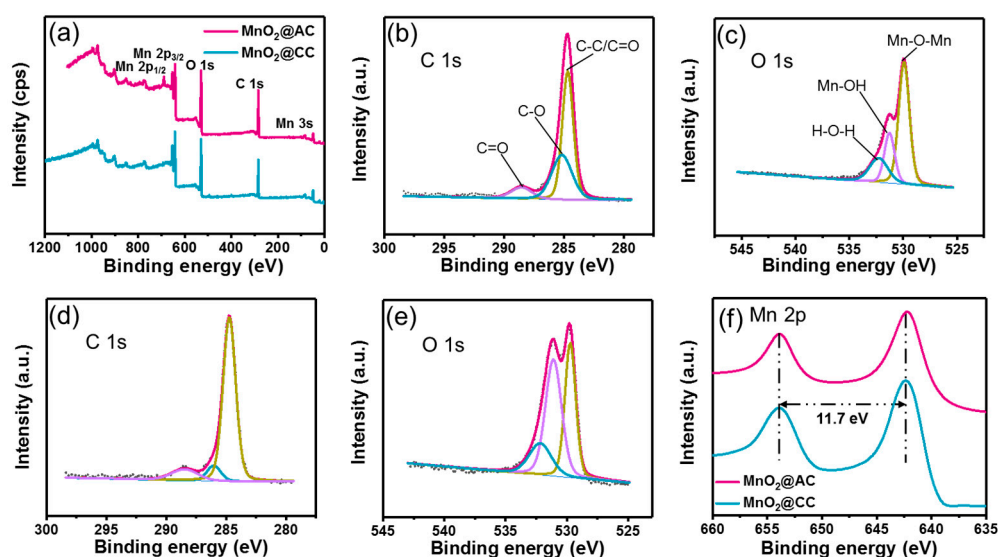


**Figure 3.** XPS spectra of  $MnO_2@AC$  and  $MnO_2@CC$ . (a) Survey XPS spectra. High-resolution spectra of  $MnO_2@AC$ : (b) C 1s peaks and (c) O 1s peaks. High-resolution spectra of  $MnO_2@CC$ : (d) C 1s peaks and (e) O 1s peaks. (f) High-resolution Mn 2p spectra.

### 3.3. Electrochemical Studies

#### 3.3.1. Capacitance Performance of $MnO_2@AC$

The electrochemical properties of the AC and  $MnO_2@AC$  electrodes were studied using a three-electrode system in a 1 M  $Na_2SO_4$  aqueous solution. The AC and  $MnO_2@AC$  electrodes both possessed good reversibility. As shown in Figure 4a, the CV curves of both AC and  $MnO_2@AC$  electrodes exhibit a rectangular shape, indicating an ideal capacitive behavior [41–44]. The integral area of CV curves of  $MnO_2@AC$ -2 h was larger than other composites, implying the biggest electrochemical capacitance. It is noteworthy that the CV curves of  $MnO_2@AC$ -2 h deviate to a certain extent and the electrochemical impedance increased due to the high mass loading of  $MnO_2$ . In addition, the resistance–capacitance constant is one of the reasons why the deviation appeared. Moreover, the nearly triangular GCD (Figure 4b) of AC and  $MnO_2@AC$  electrode indicate a high coulombic efficiency and an excellent electrochemical reversibility. As shown in Figure 4c, the GCD curves also exhibit quasi-triangular shapes, even at a high current density of  $20 \text{ mA cm}^{-2}$ , which means the  $MnO_2@AC$  electrode had good rate capability. The current response was enhanced when the mass loading of  $MnO_2$  was increasing, which indicated that the areal specific capacitance of AC increased for a certain degree after  $MnO_2$  deposition but not significantly, probably due to the blockage of the pores. It can be seen that the specific capacitance of  $MnO_2@AC$ -5 min increased by 5.1% at  $1 \text{ mA cm}^{-2}$  and that of



MnO<sub>2</sub>@AC-2 h increased by only 62.7%, 29.9%, and 12.2% compared to AC at a current density of 1, 10, and 20 mA cm<sup>-2</sup>, respectively. It even decreased at a current density of 30 mA cm<sup>-2</sup> (Figure 4d). The maximum specific capacitance of MnO<sub>2</sub>@AC reached 1281.3 mF cm<sup>-2</sup> with a 2 h deposition.

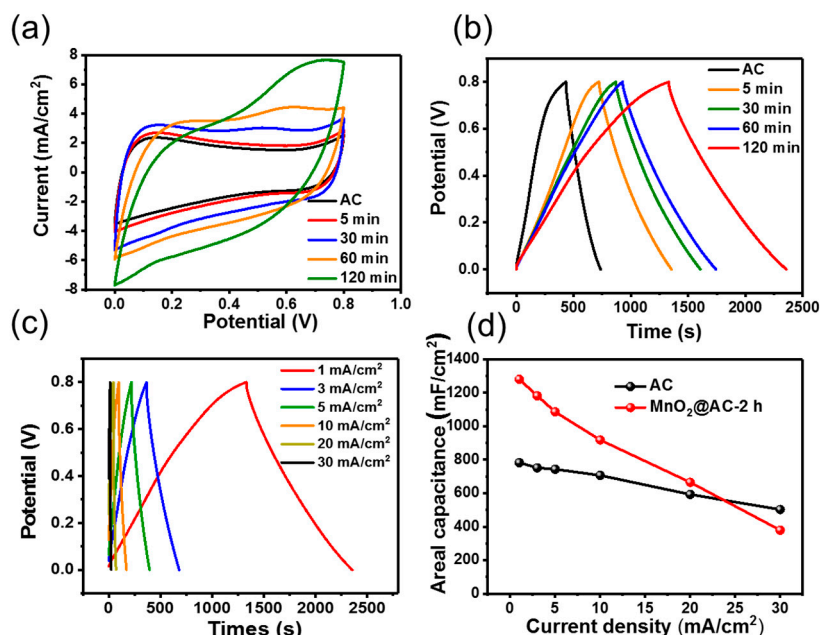


**Figure 4.** Electrochemical performance of the MnO<sub>2</sub>@AC and AC electrodes: (a) CV curves of MnO<sub>2</sub>@AC with different deposition times at a scan rate of 5 mV s<sup>-1</sup>. (b) Charge-discharge profiles of MnO<sub>2</sub>@AC with different deposition times at a current density of 1 mA/cm<sup>2</sup>. (c) Charge-discharge profiles of MnO<sub>2</sub>@AC-2 h at different current densities. (d) The area-specific capacitance of MnO<sub>2</sub>@AC.

### 3.3.2. Capacitance Performance of MnO<sub>2</sub>@CC

The three-electrode electrochemical properties of the CC and MnO<sub>2</sub>@CC electrodes are shown in Figure 5a. The CV loops of MnO<sub>2</sub>@CC electrode show quasi-rectangular shapes, suggesting an ideal pseudocapacitive behavior. This can be proved again via the triangular and symmetrical linear GCD curves (Figure 5b). Furthermore, as shown in Figure 5c, quasi-triangular shapes and a small IR drop (ohmic potential loss) of the GCD curves at different current densities indicates that the MnO<sub>2</sub>@CC electrode had a small electric resistance and a good rate stability, respectively. The electrodeposited MnO<sub>2</sub>@CC-10 h had a very high area specific capacitance (Figure 5d), which could reach up to 4475, 4293, 3660, and 2425 mF cm<sup>-2</sup> at a current density of 1, 5, 10, 20, and 30 mA cm<sup>-2</sup>, respectively. According to our knowledge, this is one of the highest values ever reported for MnO<sub>2</sub>-based materials (Figure S6) [45–53]. At the same time, compared with CC, the area-specific capacitance of MnO<sub>2</sub>@CC could be significantly increased by 8.97, 17.9, 22.4, 22.4, and 16.6 times, which was much higher than that of AC. Based on the superior area-specific capacitance, we chose the MnO<sub>2</sub>@CC-10 h as the cathode to construct the ASCs.



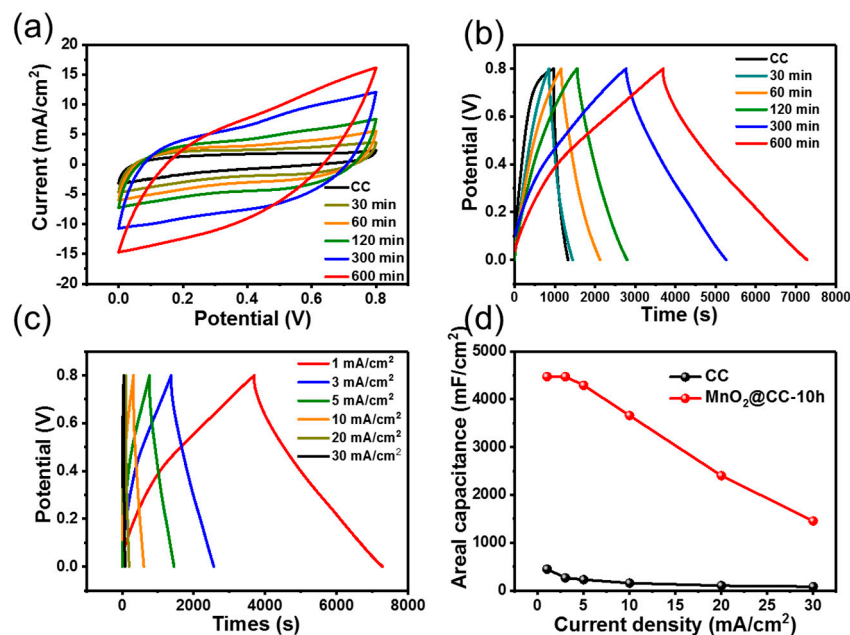


**Figure 5.** Electrochemical performance of the  $\text{MnO}_2@\text{CC}$  electrode: (a) CV curves of  $\text{MnO}_2@\text{CC}$  with different deposition times at scan rate of  $5 \text{ mV s}^{-1}$ . (b) Charge–discharge profiles of  $\text{MnO}_2@\text{CC}$  with different deposition times at a current density of  $1 \text{ mA/cm}^2$ . (c) Charge–discharge profiles of  $\text{MnO}_2@\text{CC-10 h}$  at different current densities. (d) The area-specific capacitance of  $\text{MnO}_2@\text{CC}$ .

### 3.3.3. Capacitance Performance of ASC

Sandwich-like ASCs were fabricated using AC as an anode,  $\text{MnO}_2@\text{CC}$  as a cathode, membrane filter as a separator, and PVA/LiCl gel as an electrolyte. AC was selected to balance the charge of  $\text{MnO}_2@\text{CC}$  electrode for its high capacitance value in the negative potential window. Figure 6a shows that the cell voltage of the ASCs could be extended up to 1.8 V by combining the opposite potential ranges of the AC anode and  $\text{MnO}_2@\text{CC}$  cathode. The assembled ASCs show an ideal capacitive behavior, whose CV loops shapes still remained rectangular, even at the high scan rates (Figure 6b). At different current loads, the CV curves of ASCs still show quasi-rectangular shapes and the galvanostatic charge–discharge curves (Figure 6c) are symmetrical and linear, which suggests the charges in ACSs could be transported quickly and the rate capability was good. Figure 6d shows the negative correlation between the scan rate and the area-specific capacitance of ACSs. A high areal capacitance of  $3455.6 \text{ mF cm}^{-2}$  could be obtained at a current density of  $1 \text{ mA cm}^{-2}$ .

Moreover, the ASCs assembled by AC and  $\text{MnO}_2@\text{CC}$  had the advantages of good environmental friendliness, good biocompatibility, and low production cost. In addition, the unique multi-channel design of ASCs endowed it with very high energy and power density: the maximum energy density could be  $1.56 \text{ mW h cm}^{-2}$  when the power density was  $900 \text{ mW cm}^{-2}$  and the maximum power density was  $18,000 \text{ mW cm}^{-2}$  when the energy density was  $0.249 \text{ mW h cm}^{-2}$  (Figure 6e). Furthermore, the cycling stability of the ASCs was investigated using the galvanostatic charge–discharge testing over a potential of  $-1$  and  $0.8 \text{ V}$  in the land-battery testing system (Figure 6f). After 10,000 cycles, the specific capacitance retention ratio of the as-fabricated asymmetric supercapacitor was still over 99%, displaying an excellent long-term cycling durability. Both electrochemical double-layer capacitance and pseudocapacitance behaviors showed up in the ASC. Therefore, the  $\text{MnO}_2@\text{CC}$  material demonstrated a great potential as a power source in high-performance energy storage devices.

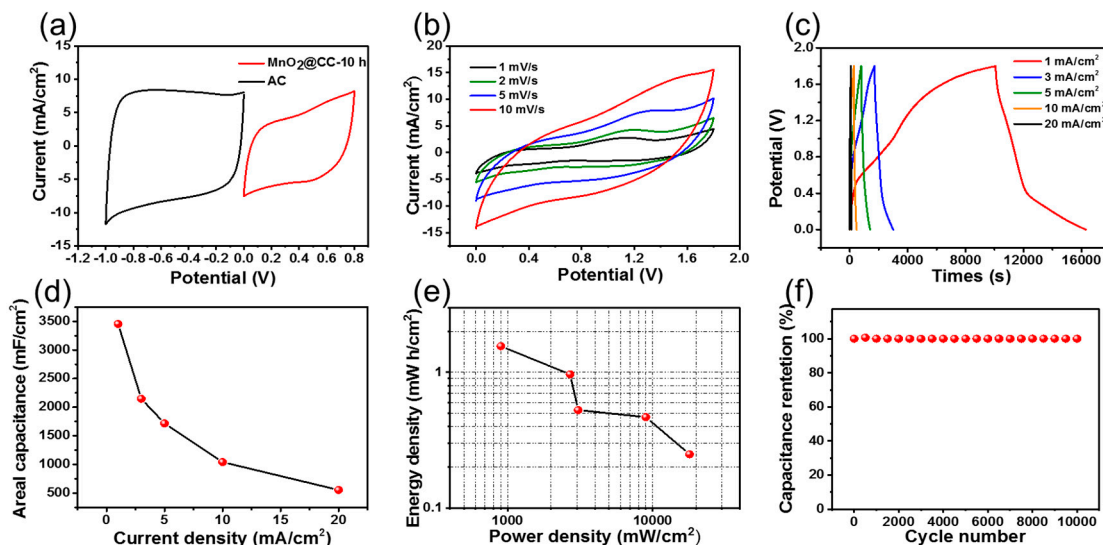


**Figure 6.** Electrochemical performance of the AC//sulfonated membrane separator//MnO<sub>2</sub>@CC ASC. (a) Typical CV curves of the AC anode and MnO<sub>2</sub>@CC cathode in the potential range of −1 to 0.8 V. (b) CV curves at various scan rates. (c) Charge–discharge profiles at different current densities. (d) Area-specific capacitance. (e) Areal energy and power densities of the ACS device. (f) Cycling stability of the ASC.

#### 4. Conclusions

In summary, we have prepared two corncob-derived carbon electrode materials with different pore structures and brought some new understanding regarding the MnO<sub>2</sub>-functionalized biomass carbon materials. We found that the effect of MnO<sub>2</sub> highly depends on the architecture of the carbon materials. For those composed by micropores with big surface area, the deposition of MnO<sub>2</sub> was fast, and easily led to clogged microstructures. On the contrary, the less-processed biomass carbon materials with a natural architecture of raw materials made a better precursor for MnO<sub>2</sub> deposition. Coupling with the synergistic effects of CC and MnO<sub>2</sub>, the obtained MnO<sub>2</sub>@CC had ultrahigh area-specific capacitance and the ASCs exhibited high energy density and good cycle stability. This work provides a new strategy to effectively improve the electrochemical performance of biomass electrode materials via the electrodeposition of MnO<sub>2</sub>.

**Supplementary Materials:** The following are available online at <http://www.mdpi.com/1996-1944/12/15/2379/s1>. Figure S1: SEM images of the natural corncob (a), AC (b), and different magnified images of CC (c,d). Figure S2: (a–c) SEM images of MnO<sub>2</sub>@AC with different electrodeposition times: 5 min (a), 30 min (b), and 120 min (c). (d–f) HR-SEM images of MnO<sub>2</sub>@AC with different electrodeposition times: 5 min (d), 30 min (e), and 120 min (f). Figure S3: SEM images of MnO<sub>2</sub>@CC with different deposition time. (a–c) SEM images of MnO<sub>2</sub>@CC-0.5 h with different magnification. (d–f) SEM images of MnO<sub>2</sub>@CC-2 h with different magnification. (g–i) SEM images of MnO<sub>2</sub>@CC-10 h with different magnification. Figure S4: (a–e) SEM images of MnO<sub>2</sub>@CC-5 h. (a) top view, (b) magnified image of (a), (c) cross-sectional view, (d) side view, and (e) magnified image of (d). (f) TEM images of MnO<sub>2</sub>@CC-5 h. Figure S5: (a) XRD patterns of AC and CC-based materials. (b) Raman spectrum of corncob-based carbon materials. Figure S6: Areal capacitance of MnO<sub>2</sub>@CC electrode compared with previously reported electrode materials [1–9].

**Author Contributions:** X.-S.L. performed the experiments; X.-S.L., Y.Y., and Q.-B.H. analyzed the data; the paper was written under the direction and supervision of M.-M.X., X.-Y.W., J.-L.R., and X.-H.W.; X.-S.L. is responsible for the writing of this work.

**Funding:** This work was financially supported by grants from the National Science Foundation of China (51673072).

**Conflicts of Interest:** The authors declare no conflict of interest.

## References

- Choi, J.-H.; Lee, C.; Cho, S.; Moon, G.D.; Kim, B.-S.; Chang, H.; Jang, H.D. High capacitance and energy density supercapacitor based on biomass-derived activated carbons with reduced graphene oxide binder. *Carbon* **2018**, *132*, 16–24. [[CrossRef](#)]
- Cao, W.; Zhang, E.; Wang, J.; Liu, Z.; Ge, J.; Yu, X.; Yang, H.; Lu, B. Potato derived biomass porous carbon as anode for potassium ion batteries. *Electrochim. Acta* **2019**, *293*, 364–370. [[CrossRef](#)]
- Chen, X.; Chi, M.; Xing, L.; Xie, X.; Liu, S.; Liang, Y.; Zheng, M.; Hu, H.; Dong, H.; Liu, Y.; et al. Natural Plant Template-Derived Cellular Framework Porous Carbon as a High-Rate and Long-Life Electrode Material for Energy Storage. *ACS Sustain. Chem. Eng.* **2019**, *7*, 5845–5855. [[CrossRef](#)]
- Wu, F.; Zhang, M.; Bai, Y.; Wang, X.; Dong, R.; Wu, C. Lotus Seedpod-Derived Hard Carbon with Hierarchical Porous Structure as Stable Anode for Sodium-Ion Batteries. *ACS Appl. Mater. Interfaces* **2019**, *11*, 12554–12561. [[CrossRef](#)] [[PubMed](#)]
- Han, J.; Zhang, L.; Zhao, B.; Qin, L.; Wang, Y.; Xing, F. The N-doped activated carbon derived from sugarcane bagasse for CO<sub>2</sub> adsorption. *Ind. Crops Prod.* **2019**, *128*, 290–297. [[CrossRef](#)]
- He, D.; Zhao, W.; Li, P.; Sun, S.; Tan, Q.; Han, K.; Liu, L.; Liu, L.; Qu, X. Bifunctional biomass-derived N, S dual-doped ladder-like porous carbon for supercapacitor and oxygen reduction reaction. *J. Alloy. Compd.* **2019**, *773*, 11–20. [[CrossRef](#)]
- Shen, H.; Zhang, Y.; Song, X.; Liu, Y.; Wang, H.; Duan, H.; Kong, X. Facile hydrothermal synthesis of actinaria-shaped  $\alpha$ -MnO<sub>2</sub>/activated carbon and its electrochemical performances of supercapacitor. *J. Alloy. Compd.* **2019**, *770*, 926–933. [[CrossRef](#)]
- Yang, G.; Park, S.-J. MnO<sub>2</sub> and biomass-derived 3D porous carbon composites electrodes for high performance supercapacitor applications. *J. Alloy. Compd.* **2018**, *741*, 360–367. [[CrossRef](#)]
- Wang, J.-G.; Kang, F.; Wei, B. Engineering of MnO<sub>2</sub>-based nanocomposites for high-performance supercapacitors. *Prog. Mater. Sci.* **2015**, *74*, 51–124. [[CrossRef](#)]
- Dai, C.; Wan, J.; Yang, J.; Qu, S.; Jin, T.; Ma, F.; Shao, J. H<sub>3</sub>PO<sub>4</sub> solution hydrothermal carbonization combined with KOH activation to prepare argy wormwood-based porous carbon for high-performance supercapacitors. *Appl. Surf. Sci.* **2018**, *444*, 105–117. [[CrossRef](#)]
- Dong, X.; Jin, H.; Wang, R.; Zhang, J.; Feng, X.; Yan, C.; Chen, S.; Wang, S.; Wang, J.; Lu, J. High Volumetric Capacitance, Ultralong Life Supercapacitors Enabled by Waxberry-Derived Hierarchical Porous Carbon Materials. *Adv. Energy Mater.* **2018**, *8*, 1702695. [[CrossRef](#)]
- Hou, J.; Cao, C.; Idrees, F.; Ma, X. Hierarchical Porous Nitrogen-Doped Carbon Nanosheets Derived from Silk for Ultrahigh-Capacity Battery Anodes and Supercapacitors. *ACS Nano* **2015**, *9*, 2556–2564. [[CrossRef](#)] [[PubMed](#)]
- Hu, B.; Wang, K.; Wu, L.; Yu, S.-H.; Antonietti, M.; Titirici, M.-M. Engineering Carbon Materials from the Hydrothermal Carbonization Process of Biomass. *Adv. Mater.* **2010**, *22*, 813–828. [[CrossRef](#)] [[PubMed](#)]
- Han, H.; Noh, Y.; Kim, Y.; Jung, W.S.; Park, S.; Kim, W.B. An N-doped porous carbon network with a multidirectional structure as a highly efficient metal-free catalyst for the oxygen reduction reaction. *Nanoscale* **2019**, *11*, 2423–2433. [[CrossRef](#)] [[PubMed](#)]
- Li, X.; Guan, B.Y.; Gao, S.; Lou, X.W. A general dual-templating approach to biomass-derived hierarchically porous heteroatom-doped carbon materials for enhanced electrocatalytic oxygen reduction. *Energy Environ. Sci.* **2019**, *12*, 648–655. [[CrossRef](#)]
- Gao, J.; Shao, C.; Shao, S.; Wan, F.; Gao, C.; Zhao, Y.; Jiang, L.; Qu, L. Laser-Assisted Large-Scale Fabrication of All-Solid-State Asymmetrical Micro-Supercapacitor Array. *Small* **2018**, *14*, 1801809. [[CrossRef](#)] [[PubMed](#)]
- Zhang, X.; Li, H.; Zhang, W.; Huang, Z.; Tsui, C.P.; Lu, C.; He, C.; Yang, Y. In-situ growth of polypyrrole onto bamboo cellulose-derived compressible carbon aerogels for high performance supercapacitors. *Electrochim. Acta* **2019**, *301*, 55–62. [[CrossRef](#)]
- Kim, J.K.; Park, S.-K.; Park, J.-S.; Kang, Y.C. Uniquely structured composite microspheres of metal sulfides and carbon with cubic nanorooms for highly efficient anode materials for sodium-ion batteries. *J. Mater. Chem. A* **2019**, *7*, 2636–2645. [[CrossRef](#)]
- Fu, W.; Zhao, E.; Ren, X.; Magasinski, A.; Yushin, G. Hierarchical Fabric Decorated with Carbon Nanowire/Metal Oxide Nanocomposites for 1.6 V Wearable Aqueous Supercapacitors. *Adv. Energy Mater.* **2018**, *8*, 1703454. [[CrossRef](#)]

20. Mei, J.; Liao, T.; Kou, L.; Sun, Z. Two-Dimensional Metal Oxide Nanomaterials for Next-Generation Rechargeable Batteries. *Adv. Mater.* **2017**, *29*, 1700176. [[CrossRef](#)]
21. Peng, L.; Xiong, P.; Ma, L.; Yuan, Y.; Zhu, Y.; Chen, D.; Luo, X.; Lu, J.; Amine, K.; Yu, G. Holey two-dimensional transition metal oxide nanosheets for efficient energy storage. *Nat. Commun.* **2017**, *8*, 15139. [[CrossRef](#)] [[PubMed](#)]
22. Sun, J.; Lv, C.; Lv, F.; Chen, S.; Li, D.; Guo, Z.; Han, W.; Yang, D.; Guo, S. Tuning the Shell Number of Multishelled Metal Oxide Hollow Fibers for Optimized Lithium-Ion Storage. *ACS Nano* **2017**, *11*, 6186–6193. [[CrossRef](#)] [[PubMed](#)]
23. Duay, J.; Sherrill, S.A.; Gui, Z.; Gillette, E.; Lee, S.B. Self-Limiting Electrodeposition of Hierarchical MnO<sub>2</sub> and M(OH)<sub>2</sub>/MnO<sub>2</sub> Nanofibril/Nanowires: Mechanism and Supercapacitor Properties. *ACS Nano* **2013**, *7*, 1200–1214. [[CrossRef](#)] [[PubMed](#)]
24. Tao, X.; Wang, J.; Liu, C.; Wang, H.; Yao, H.; Zheng, G.; Seh, Z.W.; Cai, Q.; Li, W.; Zhou, G.; et al. Balancing surface adsorption and diffusion of lithium-polysulfides on nonconductive oxides for lithium-sulfur battery design. *Nat. Commun.* **2016**, *7*, 11203. [[CrossRef](#)] [[PubMed](#)]
25. Chen, L.-F.; Huang, Z.-H.; Liang, H.-W.; Guan, Q.-F.; Yu, S.-H. Bacterial-Cellulose-Derived Carbon Nanofiber@MnO<sub>2</sub> and Nitrogen-Doped Carbon Nanofiber Electrode Materials: An Asymmetric Supercapacitor with High Energy and Power Density. *Adv. Mater.* **2013**, *25*, 4746–4752. [[CrossRef](#)] [[PubMed](#)]
26. Chen, W.; Rakhi, R.B.; Hu, L.; Xie, X.; Cui, Y.; Alshareef, H.N. High-Performance Nanostructured Supercapacitors on a Sponge. *Nano Lett.* **2011**, *11*, 5165–5172. [[CrossRef](#)] [[PubMed](#)]
27. He, Y.; Chen, W.; Li, X.; Zhang, Z.; Fu, J.; Zhao, C.; Xie, E. Freestanding Three-Dimensional Graphene/MnO<sub>2</sub> Composite Networks as Ultralight and Flexible Supercapacitor Electrodes. *ACS Nano* **2013**, *7*, 174–182. [[CrossRef](#)] [[PubMed](#)]
28. Lee, J.S.; Shin, D.H.; Jang, J. Polypyrrole-coated manganese dioxide with multiscale architectures for ultrahigh capacity energy storage. *Energy Environ. Sci.* **2015**, *8*, 3030–3039. [[CrossRef](#)]
29. Yu, N.; Yin, H.; Zhang, W.; Liu, Y.; Tang, Z.; Zhu, M.-Q. High-Performance Fiber-Shaped All-Solid-State Asymmetric Supercapacitors Based on Ultrathin MnO<sub>2</sub> Nanosheet/Carbon Fiber Cathodes for Wearable Electronics. *Adv. Energy Mater.* **2016**, *6*, 1501458. [[CrossRef](#)]
30. Amir, F.Z.; Pham, V.H.; Schultheis, E.M.; Dickerson, J.H. Flexible, all-solid-state, high-cell potential supercapacitors based on holey reduced graphene oxide/manganese dioxide nanosheets. *Electrochim. Acta* **2018**, *260*, 944–951. [[CrossRef](#)]
31. Sumboja, A.; Foo, C.Y.; Wang, X.; Lee, P.S. Large areal mass, flexible and free-standing reduced graphene oxide/manganese dioxide paper for asymmetric supercapacitor device. *Adv. Mater.* **2013**, *25*, 2809–2815. [[CrossRef](#)] [[PubMed](#)]
32. Zhang, P.; Li, K.; Liu, X. Carnation-like MnO<sub>2</sub> modified activated carbon air cathode improve power generation in microbial fuel cells. *J. Power Sour.* **2014**, *264*, 248–253. [[CrossRef](#)]
33. Yuan, X.; Zhang, Y.; Yan, Y.; Wei, B.; Qiao, K.; Zhu, B.; Cai, X.; Chou, T.-W. Tunable synthesis of biomass-based hierarchical porous carbon scaffold@MnO<sub>2</sub> nanohybrids for asymmetric supercapacitor. *Chem. Eng. J.* **2019**. [[CrossRef](#)]
34. Cheng, Z.; Tan, G.; Qiu, Y.; Guo, B.; Cheng, F.; Fan, H. High performance electrochemical capacitors based on MnO<sub>2</sub>/activated-carbon-paper. *J. Mater. Chem. C* **2015**, *3*, 6166–6171. [[CrossRef](#)]
35. Fuertes, A.B.; Lota, G.; Centeno, T.A.; Frackowiak, E. Templated mesoporous carbons for supercapacitor application. *Electrochim. Acta* **2005**, *50*, 2799–2805. [[CrossRef](#)]
36. Bao, L.; Li, X. Towards textile energy storage from cotton T-shirts. *Adv. Mater.* **2012**, *24*, 3246–3252. [[CrossRef](#)] [[PubMed](#)]
37. Chen, W.; Rakhi, R.B.; Wang, Q.; Hedhili, M.N.; Alshareef, H.N. Morphological and Electrochemical Cycling Effects in MnO<sub>2</sub> Nanostructures by 3D Electron Tomography. *Adv. Funct. Mater.* **2014**, *24*, 3130–3143. [[CrossRef](#)]
38. Xu, H.; Hu, X.; Sun, Y.; Yang, H.; Liu, X.; Huang, Y. Flexible fiber-shaped supercapacitors based on hierarchically nanostructured composite electrodes. *Nano Res.* **2014**, *8*, 1148–1158. [[CrossRef](#)]
39. Wang, X.; Chen, S.; Li, D.; Sun, S.; Peng, Z.; Komarneni, S.; Yang, D. Direct Interfacial Growth of MnO<sub>2</sub> Nanostructure on Hierarchically Porous Carbon for High-Performance Asymmetric Supercapacitors. *ACS Sustain. Chem. Eng.* **2018**, *6*, 633–641. [[CrossRef](#)]



40. Zhang, Z.; Xiao, F.; Qian, L.; Xiao, J.; Wang, S.; Liu, Y. Facile Synthesis of 3D MnO<sub>2</sub>-Graphene and Carbon Nanotube-Graphene Composite Networks for High-Performance, Flexible, All-Solid-State Asymmetric Supercapacitors. *Adv. Energy Mater.* **2014**, *4*, 1400064. [\[CrossRef\]](#)
41. Brousse, T.; Toupin, M.; Dugas, R.; Athouël, L.; Crosnier, O.; Beéanger, D. Crystalline MnO<sub>2</sub> as Possible Alternatives to Amorphous Compounds in Electrochemical Supercapacitors. *J. Electrochem. Soc.* **2006**, *153*, 2171–2180. [\[CrossRef\]](#)
42. Ghodbane, O.; Pascal, J.-L.; Favier, F. Microstructural Effects on Charge-Storage Properties in MnO<sub>2</sub>-Based Electrochemical Supercapacitors. *ACS Appl. Mater. Interfaces* **2009**, *1*, 1130–1139. [\[CrossRef\]](#) [\[PubMed\]](#)
43. Hu, C.-C.; Tsou, T.-W. Ideal capacitive behavior of hydrous manganese oxide prepared by anodic deposition. *Electrochem. Commun.* **2002**, *4*, 105–109. [\[CrossRef\]](#)
44. Zhao, D.; Chen, C.; Zhang, Q.; Chen, W.; Liu, S.; Wang, Q.; Liu, Y.; Li, J.; Yu, H. High Performance, Flexible, Solid-State Supercapacitors Based on a Renewable and Biodegradable Mesoporous Cellulose Membrane. *Adv. Energy Mater.* **2017**, *7*, 1700739. [\[CrossRef\]](#)
45. Dubal, D.P.; Aradilla, D.; Bidan, G.; Gentile, P.; Schubert, T.J.S.; Wimberg, J.; Sadki, S.; Gomez-Romero, P. 3D hierarchical assembly of ultrathin MnO<sub>2</sub> nanoflakes on silicon nanowires for high performance micro-supercapacitors in Li- doped ionic liquid. *Sci. Rep.* **2015**, *5*, 9771. [\[CrossRef\]](#)
46. Hu, L.; Chen, W.; Xie, X.; Liu, N.; Yang, Y.; Wu, H.; Yao, Y.; Pasta, M.; Alshareef, H.N.; Cui, Y. Symmetrical MnO<sub>2</sub>-Carbon Nanotube-Textile Nanostructures for Wearable Pseudocapacitors with High Mass Loading. *ACS Nano* **2011**, *5*, 8904–8913. [\[CrossRef\]](#) [\[PubMed\]](#)
47. Li, Y.; Yu, N.; Yan, P.; Li, Y.; Zhou, X.; Chen, S.; Wang, G.; Wei, T.; Fan, Z. Fabrication of manganese dioxide nanoplates anchoring on biomass-derived cross-linked carbon nanosheets for high-performance asymmetric supercapacitors. *J. Power Sour.* **2015**, *300*, 309–317. [\[CrossRef\]](#)
48. Mai, L.-Q.; Yang, F.; Zhao, Y.-L.; Xu, X.; Xu, L.; Luo, Y.-Z. Hierarchical MnMoO<sub>4</sub>/CoMoO<sub>4</sub> heterostructured nanowires with enhanced supercapacitor performance. *Nat. Commun.* **2011**, *2*, 381. [\[CrossRef\]](#)
49. Wu, P.; Cheng, S.; Yang, L.; Lin, Z.; Gui, X.; Ou, X.; Zhou, J.; Yao, M.; Wang, M.; Zhu, Y.; et al. Synthesis and Characterization of Self-Standing and Highly Flexible δ-MnO<sub>2</sub>@CNTs/CNTs Composite Films for Direct Use of Supercapacitor Electrodes. *ACS Appl. Mater. Interfaces* **2016**, *8*, 23721–23728. [\[CrossRef\]](#)
50. Xu, H.; Hu, X.; Yang, H.; Sun, Y.; Hu, C.; Huang, Y. Flexible Asymmetric Micro-Supercapacitors Based on Bi<sub>2</sub>O<sub>3</sub> and MnO<sub>2</sub> Nanoflowers: Larger Areal Mass Promises Higher Energy Density. *Adv. Energy Mater.* **2015**, *5*, 1401882. [\[CrossRef\]](#)
51. Yu, G.; Hu, L.; Liu, N.; Wang, H.; Vosgueritchian, M.; Yang, Y.; Cui, Y.; Bao, Z. Enhancing the Supercapacitor Performance of Graphene/MnO<sub>2</sub> Nanostructured Electrodes by Conductive Wrapping. *Nano Lett.* **2011**, *11*, 4438–4442. [\[CrossRef\]](#) [\[PubMed\]](#)
52. Yuan, L.; Lu, X.-H.; Xiao, X.; Zhai, T.; Dai, J.; Zhang, F.; Hu, B.; Wang, X.; Gong, L.; Chen, J.; et al. Flexible Solid-State Supercapacitors Based on Carbon Nanoparticles/MnO<sub>2</sub> Nanorods Hybrid Structure. *ACS Nano* **2012**, *6*, 656–661. [\[CrossRef\]](#) [\[PubMed\]](#)
53. Chen, C.; Zhang, Y.; Li, Y.; Dai, J.; Song, J.; Yao, Y.; Gong, Y.; Kierzewski, I.; Xie, J.; Hu, L. All-wood, low tortuosity, aqueous, biodegradable supercapacitors with ultra-high capacitance. *Energy Environ. Sci.* **2017**, *10*, 538–545. [\[CrossRef\]](#)

